Mineralogical Magazine, August 2016, Vol. 80(5), pp. 901–914

Crystal structure of adamite at high temperature

M. Zema[1,2,*], S. C. Tarantino[1,2], M. Boiocchi[3] and A. M. Callegari[1]

[1] Dipartimento di Scienze della Terra e dell'Ambiente, Università degli Studi di Pavia, via Ferrata 9, I-27100 Pavia, Italy
[2] CNR-IGG, Sezione di Pavia, via Ferrata 9, I-27100 Pavia, Italy
[3] Centro Grandi Strumenti, Università di Pavia, via Bassi 21, I-27100 Pavia, Italy

[*Received 12 July 2015; Accepted 4 September 2015; Associate Editor: Stuart Mills*]

ABSTRACT

Structural modifications with temperature of adamite, $Zn_2(AsO_4)(OH)$, were determined by single-crystal X-ray diffraction up to dehydration and collapse of the crystal structure. In the temperature range 25–400°C, adamite shows positive and linear expansion. Axial thermal expansion coefficients, determined over this temperature range, are $\alpha_a = 1.06(2) \times 10^{-5}$ K^{-1}, $\alpha_b = 1.99(2) \times 10^{-5}$ K^{-1}, $\alpha_c = 3.7(1) \times 10^{-6}$ K^{-1} and $\alpha_V = 3.43(3) \times 10^{-5}$ K^{-1}. Axial expansion is then strongly anisotropic with α_a:α_b:α_c = 2.86: 5.38 : 1. Structure refinements of X-ray diffraction data collected at different temperatures allowed us to characterize the mechanisms by which the adamite structure accommodates variations in temperature. Expansion is limited mainly by edge sharing Zn(2) dimers along *a* and by edge sharing Zn(1) octahedra chains along *c*; on the other hand, connections of polyhedra along *b*, the direction of maximum expansion, is governed by corner sharing. Increasing temperature induces mainly an axial expansion of Zn(1) octahedron, which becomes more elongated, and no significant variations of the Zn(2) trigonal bipyramids and As tetrahedra. Starting from 400°C, deviation from a linear evolution of unit-cell parameters is observed, associated with some deterioration of the crystal, a sign of incipient dehydration. The process leads to the formation of $Zn_4(AsO_4)_2O$.

Keywords: adamite, thermal expansion, single-crystal X-ray diffraction.

Introduction

Adamite, $Zn_2(AsO_4)(OH)$ is a widespread secondary mineral, typical of the oxidation zone of zinc deposits containing arsenic minerals. It is a member of the olivenite group following the new Dana classification (Gaines *et al.*, 1997), together with other arsenate and phosphate minerals, such as eveite, olivenite, zincolivenite, libethenite and zincolibethenite. Members of this group crystallize in the orthorhombic *Pnnm* space group with the exception of olivenite ($P2_1/n$). Recently, a new member of the group, auriacusite, the Fe^{3+}-analogue of zincolivenite, was reported (Mills *et al.*, 2010). Among the minerals of the olivenite group, adamite is the most common. It was considered as a member of the olivenite group based on morphological and chemical considerations, until Kokkoros (1937) reported the first two-dimensional crystal-structure analysis of a crystal from Laurion, based on less than 100 X-ray reflections. Later, the adamite crystal structure was refined by Hill (1976) and, nearly at the same time, by Hawthorne (1976) and Kato and Miura (1977) using single-crystal X-ray diffraction data. A study of the olivenite–adamite solid solution was carried out by Toman (1978). More recently, adamite has been characterized by spectroscopic (IR and Raman) and quantum theoretical methods (Makreski *et al.*, 2013).

The crystal structure of adamite (Fig. 1) can be derived from that of andalusite, and consists of two independent Zn ions, Zn(1) and Zn(2), occurring in six- or five-fold coordination, and defining

* E-mail: michele.zema@unipv.it
DOI: 10.1180/minmag.2016.080.030

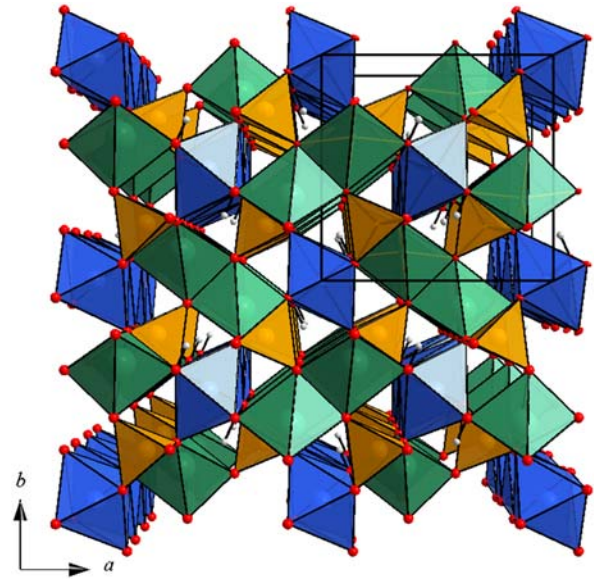

FIG. 1. Perspective view of the crystal structure of adamite plotted along *c*. Thermal ellipsoids are plotted at 50% probability level. Light blue: Zn(1) octahedra forming straight chains along *c*; green: Zn(2) trigonal bipyramids forming isolated dimers occupying channels running along *c*; orange: As tetrahedra. Hydrogen atoms are coloured grey.

TABLE 1. Crystal data and details of CCD data collection and structure refinement of adamite at room temperature.

a (Å)	8.5312(3)
b (Å)	8.3149(3)
c (Å)	6.0590(2)
V (Å^3)	429.80(3)
Z	4
μ Mo*K*α (mm^{-1})	18.71
θ max	38.54
F_{000}	536
h range	–14 to 14
k range	–14 to 14
l range	–10 to 10
Reflections measured	10,139
Reflections unique	1271
Reflections observed ($I > 2\sigma_I$)	1215
R_{int} (%)	4.14
R_1^a (%)	2.07
R_{all}^a (%)	2.17
wR_2 (%)	5.51
Goof[b]	1.214
Largest diff. peak/hole (*e* Å^{-3})	1.47, –1.32

[a]$R = \Sigma \, ||F_o| - |F_c|| \, / \, \Sigma \, |F_o|$ (R_1 is calculated on reflections with $I > 2\sigma_I$).
[b]Goof = $S = [\Sigma \, [w(F_o^2 - F_c^2)^2] \, / \, (n-p)]^{0.5}$, where *n* is the number of reflections and *p* is the total number of parameters refined.

$ZnO_4(OH)_2$ octhahedra and $ZnO_4(OH)$ trigonal bipyramids, respectively. The Zn(1) ions are connected to two of each O1, O2 and O4 oxygen atoms, O4 being the hydroxyl group. The Zn(1)–O1 bond lengths are longer than the others, and the coordination can be considered as a 4 + 2 type. Zinc octahedra share edges (alternately, O2–O2 and O4–O4) to form chains parallel to *c*, and share corners (O4 and O1) with $ZnO_4(OH)$ trigonal bipyramids in the *a* and *b* directions. Octahedral chains also share corners (O1 and O2) with isolated AsO_4 tetrahedra, which have almost regular geometry. These tetrahedra crosslink two Zn polyhedra to produce a dense framework structure in which all O atoms and OH groups are trigonally coordinated. The penta-coordinate Zn(2) ions are connected to two O1 and O3 atoms and one O4. Such polyhedra form dimers by sharing the O3–O3 edge, and are connected with As tetrahedra through O1 and O3 atoms. To reduce the high-energy effects of edge sharing, shortening of the shared edge occurs.

The aim of the present work was to study the structural behaviour of adamite upon thermal treatment by *in situ* high temperature (HT) single-crystal X-ray diffraction (SC-XRD), from room temperature (RT) up to dehydration and transformation into anhydrous zinc arsenate, with collapse of the crystal

https://doi.org/10.1180/minmag.2016.080.030 Published online by Cambridge University Press

TABLE 2. Unit-cell parameters of adamite at different temperatures.

T (°C)	a (Å)	b (Å)	c (Å)	V (Å^3)
Stage 1				
25	8.5234(5)	8.3080(5)	6.0555(4)	428.81(5)
50	8.5244(5)	8.3109(4)	6.0559(3)	429.04(4)
75	8.5262(4)	8.3150(5)	6.0563(3)	429.37(4)
100	8.5286(5)	8.3203(5)	6.0570(3)	429.81(4)
125	8.5312(5)	8.3236(5)	6.0572(3)	430.13(4)
150	8.5331(5)	8.3277(5)	6.0578(3)	430.47(4)
175	8.5343(5)	8.3310(5)	6.0586(4)	430.76(4)
200	8.5369(4)	8.3356(4)	6.0589(3)	431.15(4)
225	8.5403(5)	8.3406(4)	6.0594(3)	431.62(4)
250	8.5421(4)	8.3449(5)	6.0597(3)	431.95(4)
275	8.5443(6)	8.3499(7)	6.0604(3)	432.37(5)
300	8.5469(5)	8.3535(5)	6.0609(3)	432.73(4)
325	8.5504(6)	8.3564(6)	6.0619(3)	433.12(5)
350	8.5506(7)	8.3607(5)	6.0629(4)	433.43(5)
375	8.5546(9)	8.3651(9)	6.0631(4)	433.88(7)
400	8.5555(8)	8.3685(6)	6.0640(4)	434.16(6)
400[a]	8.5561(6)	8.3686(5)	6.0664(6)	434.37(6)
425	8.5570(7)	8.3729(6)	6.0683(5)	434.78(6)
450	8.5590(7)	8.3761(8)	6.0686(5)	435.06(6)
475	8.5599(8)	8.3802(8)	6.0739(6)	435.70(7)
500	8.5611(14)	8.3756(16)	6.0750(9)	435.60(13)
Stage 2				
25	8.5133(24)	8.3078(21)	6.0554(12)	428.28(18)
100	8.5188(25)	8.3170(22)	6.0580(10)	429.22(18)
200	8.5278(22)	8.3311(23)	6.0619(10)	430.67(18)
300	8.5382(31)	8.3437(32)	6.0663(11)	432.17(24)
400	8.5457(29)	8.3586(31)	6.0706(14)	433.62(24)
500	8.5526(34)	8.3765(40)	6.0742(12)	435.16(28)

[a]Measured 10 min after the end of the previous measurement.

TABLE 3. Details of HT data collections and structure refinements for adamite.

T (°C)	RT	100	200	300	400	500
Refl. measured	1321	946	951	953	955	500
Refl. unique	686	491	494	495	496	500
Average I/σ_I	32.36	36.70	35.00	33.87	32.72	27.62
R_{int} (%)	9.40	6.04	5.74	5.55	5.63	n.d.[c]
Refl. with $I > 2\sigma_I$	612	427	424	422	423	405
R_1^a (%)	4.19	3.70	3.52	3.58	3.56	8.25
R_{all}^a (%)	4.56	4.24	4.10	4.33	4.40	9.41
wR_2 (%)	14.16	10.59	9.27	9.47	9.00	23.37
Goof[b]	1.275	1.368	1.283	1.351	1.251	1.124
max Δρ (e Å^{-3})	1.89	1.03	0.73	0.85	0.84	2.68
min Δρ (e Å^{-3})	–1.79	–1.12	–1.02	–0.93	–0.91	–2.07

[a]$R = \Sigma||F_o| - |F_c||/\Sigma\,|F_o|$ (R_1 is calculated on reflections with $I > 2\sigma_I$.
[b]Goof = S = $[\Sigma\,[w(F_o^2 - F_c^2)^2]/(n-p)]^{0.5}$, where n is the number of reflections and p is the total number of parameters refined.
[c]Only independent reflections were collected.

https://doi.org/10.1180/minmag.2016.080.030 Published online by Cambridge University Press

TABLE 4. Fractional coordinates and anisotropic displacement parameters U^{ij} ($\times 10^4$ Å^2) for adamite.

T (°C)	25*	25	100	200	300	400	500
Site Zn(1), Wyckoff position 4*e* (0,0,*z*)							
z/*c*	0.25263(4)	0.25275(14)	0.25250(20)	0.25284(19)	0.25272(21)	0.25290(21)	0.25297(41)
U^{11}	126(1)	245(6)	295(7)	341(6)	381(7)	427(7)	453(15)
U^{22}	150(1)	272(7)	325(10)	395(9)	462(10)	537(10)	688(19)
U^{33}	32(1)	99(5)	221(7)	235(6)	252(7)	274(6)	280(14)
U^{12}	–58(1)	–63(4)	–76(5)	–101(5)	–124(6)	–150(7)	–177(12)
U_{eq}	103(1)	205(4)	280(5)	324(5)	365(5)	413(5)	474(9)
Site Zn(2), Wyckoff position 4*g* (*x*,*y*,0)							
x/*a*	0.13574(3)	0.13567(11)	0.13608(13)	0.13629(12)	0.13663(14)	0.13689(14)	0.13709(26)
y/*b*	0.63481(3)	0.63484(12)	0.63474(15)	0.63429(15)	0.63394(16)	0.63350(16)	0.63310(29)
U^{11}	78(1)	194(5)	247(7)	267(6)	290(6)	315(7)	331(13)
U^{22}	65(1)	179(6)	197(8)	233(7)	259(8)	297(8)	428(14)
U^{33}	59(1)	124(5)	251(6)	278(6)	308(6)	339(6)	359(13)
U^{12}	1(1)	3(4)	8(5)	7(5)	7(5)	8(6)	3(10)
U_{eq}	67(1)	166(4)	232(5)	259(4)	286(4)	317(4)	373(8)
Site As(1), Wyckoff position 4*g* (*x*,*y*,0)							
x/*a*	0.24403(2)	0.24394(8)	0.24360(11)	0.24302(10)	0.24248(11)	0.24209(11)	0.24177(19)
y/*b*	0.25057(2)	0.25061(10)	0.25075(13)	0.25063(12)	0.25052(13)	0.25041(13)	0.24997(22)
U^{11}	56(1)	173(5)	207(6)	216(5)	227(5)	248(5)	250(11)
U^{22}	38(1)	163(6)	177(7)	191(7)	208(7)	232(7)	342(12)
U^{33}	32(1)	96(5)	215(6)	235(5)	251(6)	263(5)	267(12)
U^{12}	–6(1)	–7(3)	–6(4)	–9(3)	–9(4)	–12(4)	–10(7)
U_{eq}	42(1)	144(4)	200(4)	214(4)	229(4)	248(4)	286(7)
Site O1, Wyckoff position 8*h* (*x*,*y*,*z*)							
x/*a*	0.36121(14)	0.36140(48)	0.35972(58)	0.35847(55)	0.35765(60)	0.35734(60)	0.35583(117)
y/*b*	0.27024(15)	0.27172(63)	0.26949(64)	0.26860(60)	0.26864(67)	0.26789(68)	0.26792(127)
z/*c*	0.22260(20)	0.22350(64)	0.22300(88)	0.22363(81)	0.22320(87)	0.22291(84)	0.22360(183)
U^{11}	133(5)	286(21)	347(26)	389(24)	422(27)	460(28)	506(59)
U^{22}	112(4)	279(25)	220(28)	233(27)	278(30)	333(31)	494(60)
U^{33}	48(4)	95(17)	239(23)	269(22)	286(25)	304(24)	306(52)
U^{23}	24(3)	47(16)	64(24)	50(23)	65(25)	66(25)	107(47)
U^{13}	–36(3)	–47(14)	–76(22)	–82(21)	–78(24)	–97(24)	–177(45)
U^{12}	–45(4)	–44(18)	–63(23)	–64(21)	–72(24)	–76(24)	–168(46)
U_{eq}	98(2)	220(10)	269(12)	297(11)	329(13)	365(13)	435(26)

Site O2, Wyckoff position 4*g* (*x*,*y*,0)							
x/*a*	0.14450(19)	0.14429(66)	0.14407(88)	0.14380(81)	0.14248(89)	0.14141(93)	0.14236(172)
y/*b*	0.07477(19)	0.07458(88)	0.07488(100)	0.07674(93)	0.07644(100)	0.07687(98)	0.07517(172)
U^{11}	115(7)	226(28)	302(38)	332(35)	338(38)	432(41)	437(77)
U^{22}	56(5)	202(33)	219(42)	231(40)	268(42)	296(43)	330(67)
U^{33}	55(6)	108(22)	240(32)	238(29)	287(33)	297(33)	305(69)
U^{12}	–37(4)	–33(24)	–60(31)	–59(29)	–79(32)	–87(34)	–112(56)
U_{eq}	75(2)	179(12)	254(17)	267(16)	297(17)	341(18)	357(31)
Site O3, Wyckoff position 4*g* (*x*,*y*,0)							
x/*a*	0.10619(20)	0.10699(74)	0.10579(89)	0.10541(80)	0.10659(87)	0.10620(88)	0.10526(155)
y/*b*	0.39498(20)	0.39474(89)	0.39468(98)	0.39347(93)	0.39429(105)	0.39462(100)	0.39548(171)
U^{11}	70(6)	169(25)	265(35)	284(32)	292(35)	324(36)	226(60)
U^{22}	57(6)	185(32)	175(38)	187(37)	249(44)	238(40)	337(70)
U^{33}	248(9)	315(32)	482(45)	521(42)	627(53)	688(53)	668(106)
U^{12}	8(5)	–27(24)	–31(31)	–14(29)	–37(34)	–13(33)	–5(50)
U_{eq}	125(3)	223(13)	307(18)	330(17)	389(20)	416(20)	410(37)
Site O4, Wyckoff position 4*g* (*x*,*y*,0)							
x/*a*	0.37206(19)	0.37245(71)	0.37152(86)	0.37231(77)	0.37337(85)	0.37338(85)	0.37151(175)
y/*b*	0.60768(20)	0.60762(82)	0.60808(97)	0.60760(90)	0.60806(100)	0.60818(102)	0.60850(183)
U^{11}	76(6)	222(27)	290(35)	286(31)	325(35)	374(37)	411(76)
U^{22}	82(5)	183(30)	215(38)	252(37)	273(42)	341(43)	468(80)
U^{33}	64(6)	131(23)	231(31)	253(29)	288(33)	300(32)	270(66)
U^{12}	0(5)	11(24)	–28(33)	2(32)	12(35)	29(37)	20(62)
U_{eq}	74(2)	178(12)	245(16)	263(14)	295(16)	338(16)	383(32)
Site H, Wyckoff position 4*g* (*x*,*y*,0)							
x/*a*	0.418(4)	0.41406	0.44050	0.45876	0.45983	0.45688	0.43221
y/*b*	0.712(2)	0.69800	0.66843	0.64868	0.69987	0.69542	0.72536
U_{iso}	89	214	294	316	354	406	459

*CCD data.

TABLE 5. Bond distances (Å) and selected geometrical parameters.

T (°C)	25*	25	100	200	300	400	500
Zn(1) octahedron							
Zn(1)–O1 (×2)	2.253(1)	2.239(5)	2.265(5)	2.280(5)	2.288(5)	2.299(5)	2.307(9)
Zn(1)–O2 (×2)	2.061(1)	2.059(4)	2.058(5)	2.065(5)	2.058(5)	2.057(5)	2.060(10)
Zn(1)–O4 (×2)	2.059(1)	2.055(4)	2.063(5)	2.058(5)	2.057(5)	2.059(5)	2.071(11)
<Zn(1)–O>	2.124(1)	2.118(4)	2.129(5)	2.134(5)	2.135(5)	2.138(5)	2.146(10)
Volume (Å^3)	12.60	12.48	12.68	12.78	12.77	12.83	12.97
OAV	28.96	29.13	28.27	26.65	28.48	28.65	27.58
OQE	1.0117	1.0114	1.0119	1.0121	1.0131	1.0136	1.0133
O4–O4 edge	2.824(2)	2.815(13)	2.835(15)	2.823(14)	2.819(15)	2.824(15)	2.854(30)
O2–O2 edge	2.761(2)	2.754(12)	2.755(15)	2.769(14)	2.750(15)	2.741(15)	2.744(28)
O2–O4 edge	3.0451(3)	3.044(1)	3.044(1)	3.043(1)	3.045(1)	3.047(1)	3.053(2)
O2–Zn(1)–O4 (°)	95.30(5)	95.4(2)	95.2(2)	95.2(2)	95.4(2)	95.5(2)	95.3(4)
Zn(2) trigonal bipyramid							
Zn(2)–O1 (×2)	2.023(1)	2.024(4)	2.018(5)	2.015(5)	2.021(5)	2.023(5)	2.024(10)
Zn(2)–O3	2.010(2)	2.010(7)	2.014(8)	2.025(8)	2.018(9)	2.016(8)	2.009(15)
Zn(2)–O3	2.079(2)	2.083(6)	2.077(8)	2.076(7)	2.092(8)	2.093(8)	2.089(13)
Zn(2)–O4	2.029(2)	2.031(6)	2.020(8)	2.027(7)	2.035(8)	2.034(7)	2.017(16)
<Zn(2)–O>	2.033(2)	2.034(6)	2.030(7)	2.032(7)	2.037(7)	2.038(7)	2.033(14)
Volume (Å^3)	7.13	7.14	7.10	7.12	7.17	7.18	7.12
O3–O3 edge	2.517(2)	2.527(14)	2.516(16)	2.529(15)	2.537(17)	2.532(16)	2.513(28)
As tetrahedron							
As–O1 (×2)	1.687(1)	1.693(4)	1.682(5)	1.682(5)	1.680(5)	1.680(5)	1.680(10)
As–O2	1.691(2)	1.691(7)	1.692(8)	1.679(7)	1.687(8)	1.689(8)	1.693(14)
As–O3	1.681(2)	1.672(7)	1.678(8)	1.673(8)	1.671(9)	1.676(8)	1.688(14)
<As–O>	1.686(2)	1.687(6)	1.683(7)	1.679(7)	1.679(8)	1.681(8)	1.685(13)
Volume (Å^3)	2.45	2.46	2.44	2.42	2.42	2.43	2.45
TAV	9.12	9.52	7.61	7.41	6.78	7.06	4.83
TQE	1.0023	1.0025	1.0019	1.0019	1.0018	1.0018	1.0012
Cation–cation distances							
Zn(1)···Zn(1)	2.998(1)	2.994(2)	2.998(2)	2.995(2)	2.997(2)	2.998(3)	3.001(5)
Zn(2)···Zn(2)	3.223(1)	3.220(2)	3.227(2)	3.229(2)	3.235(2)	3.237(3)	3.237(5)
Possible hydrogen bonds O4–H···O1 (×2)							
O4–H (Å)	0.956(10)	0.830	0.773	0.814	1.065	1.021	1.108
O4···O1^i (Å)	2.833(2)	2.825(7)	2.849(8)	2.861(8)	2.859(8)	2.866(8)	2.892(17)
H···O1^i (Å)	2.319(28)	2.357	2.233	2.177	2.081	2.109	2.267
O4–H···O1^i (°)	113.10(3)	116.3	136.9	141.5	127.7	129.1	113.4

Symmetry codes are as in Fig. 1: (*i*) $-x+1,-y+1,\pm z$.
*CCD data (not plotted in Figures).
OAV – octahedral angular variance; OQE – octahedral quadratic elongation; TAV – tetrahedral angular variance; TQE – tetrahedral quadratic elongation.

structure. The HT data are compared with those of Xu *et al.* (2014) collected at high pressure (HP).

Experimental

SC-XRD data collection at room temperature

A small, transparent, light-green single crystal of adamite from an unknown location in Chihuahua (Mexico), with dimensions 0.24 mm × 0.20 mm × 0.36 mm, was selected from the collections of the Museum of Mineralogy of the University of Pavia (inv. no. 7539/1) for X-ray data collection and structure refinement based on optical and diffraction properties. Single-crystal diffraction data were collected at room temperature with a Bruker-AXS Smart-Apex CCD diffractometer, with graphite-monochromatized Mo$K\alpha$ radiation ($\lambda = 0.71073$ Å)

https://doi.org/10.1180/minmag.2016.080.030 Published online by Cambridge University Press

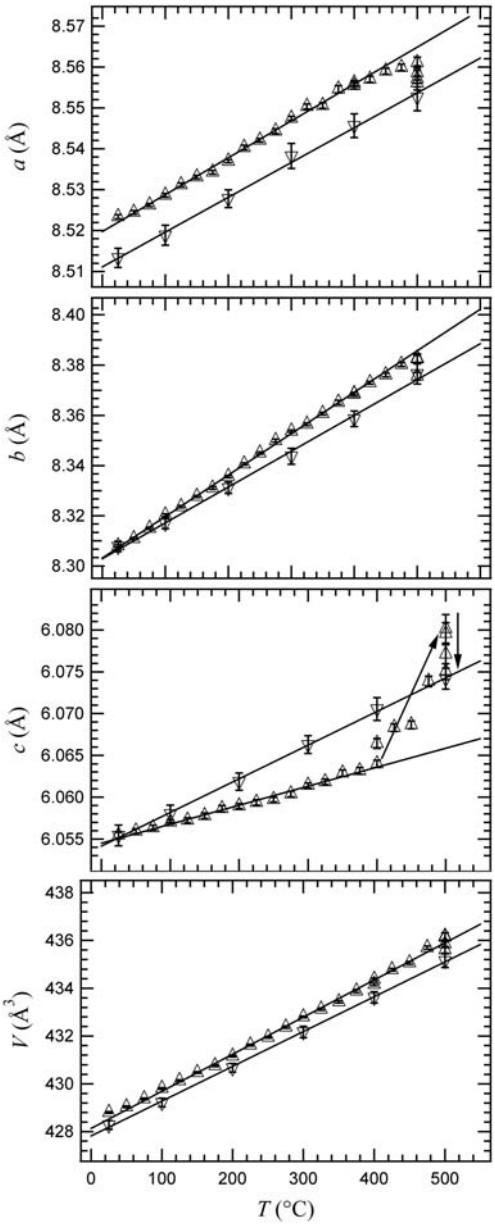

FIG. 2. Variation of unit-cell parameters and volume with temperature for adamite. Triangles up: Stage 1; triangles down: Stage 2. Linear regressions calculated in the range 25–400°C are shown as solid lines.

and operating conditions 50 kV and 30 mA. The Bruker *SMART* system of programs was used for preliminary crystal lattice determination and X-ray data collection. A total of 2240 ω-rotation frames (scan width = 0.3°ω; exposure time = 10 s/frame; detector-to-sample distance = 40 mm; resolution = 512 × 512 pixels) were collected and processed by *SAINT+* software (Bruker AXS). Intensity data were corrected for background, Lorentz and polarization effects. The semi-empirical absorption correction of Blessing (1995), based on the determination of transmission factors for equivalent reflections, was applied using the Bruker program *SADABS* (Sheldrick, 2003). Final unit-cell parameters were obtained by the Bruker *GLOBAL* least-squares orientation matrix refinement procedure, based on the positions of all measured reflections. Additional details on RT data collection are reported in Table 1.

SC-XRD at high temperature

In situ HT intensity data were collected on the same crystal used for the RT study using a Philips PW1100 four-circle diffractometer with graphite-monochromatized Mo*K*α radiation, operating at 55 kV and 30 mA. Horizontal and vertical apertures for the punctual detector were 2.0° and 1.5°, respectively. A home-made U-shaped microfurnace with a K-type thermocouple was used. Temperature was previously calibrated by known melting points, and reported temperatures are precise to within ±5°. The crystal was inserted into a sealed quartz capillary (0.3 mm diameter) and kept in position by a wad of quartz wool.

Unit-cell parameters were measured from RT up to 500°C, at steps of 25°C. At each working temperature, the orientation matrix was updated by centring a selected list of 25 reflections in the range ~6.9–12.9°θ. Accurate lattice parameters (Table 2) were then measured by a least-squares routine procedure (Philips LAT) over 52 to 55 d^* spacings, each measured considering all the reflections in the range $3° < \theta < 26°$. Complete datasets of diffracted intensities were collected at $T = 25$, 100, 200, 300, 400 and 500°C using the operating conditions reported above. The equivalent reflections hkl, $h\bar{k}l$, were measured in the range 2–26.5°θ (2–30°θ for the dataset collected at RT) by the ω/2θ scan mode for datasets collected at RT to 400°C, whereas at 500°C, due to the deterioration of the crystal and consequent decrease of diffracted intensities, only independent hkl reflections were measured. During all data collection, three standard reflections were measured every 200 reflections. X-ray diffraction intensities were obtained by measuring step-scan profiles and analysing them by the Lehman and

https://doi.org/10.1180/minmag.2016.080.030 Published online by Cambridge University Press

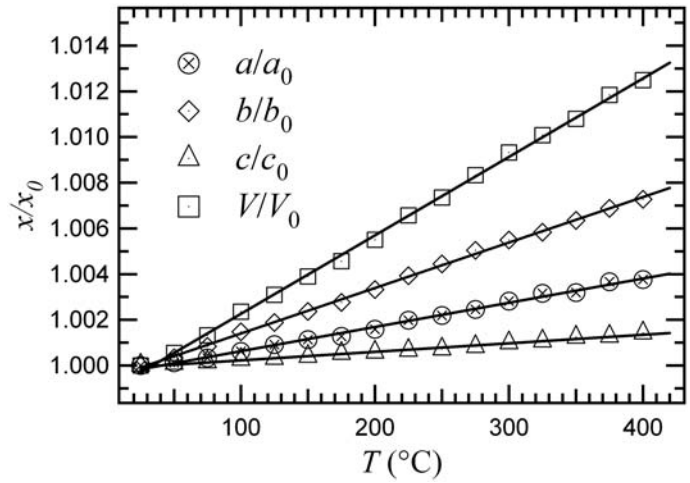

FIG. 3. Normalized unit-cell parameters and volume for adamite as a function of temperature. Linear regressions calculated in the range 25–400°C are shown as solid lines.

Larsen (1974) σ_I/I method, as modified by Blessing *et al.* (1974). Azimuthal scans were performed in order to correct data for absorption (North *et al.*, 1968). Some additional details on the HT data collections are reported in Table 3.

At the end of the data collection at 500°C, the crystal was cooled down quickly to room temperature, in order to quench the progressive deterioration. Unit-cell parameters were then measured again from RT up to 500°C, at 100°C intervals. Given the lower quality of the crystal and the consequent weakened intensities and broader profiles, unit-cell parameters were measured by the LAT routine using only 41 to 44 d^* spacings, each measured in the same θ range as above. Data are reported in Table 2 and are referred to as Stage 2. Finally, the crystal was kept at 550°C for a further 6 h to effect complete dehydration.

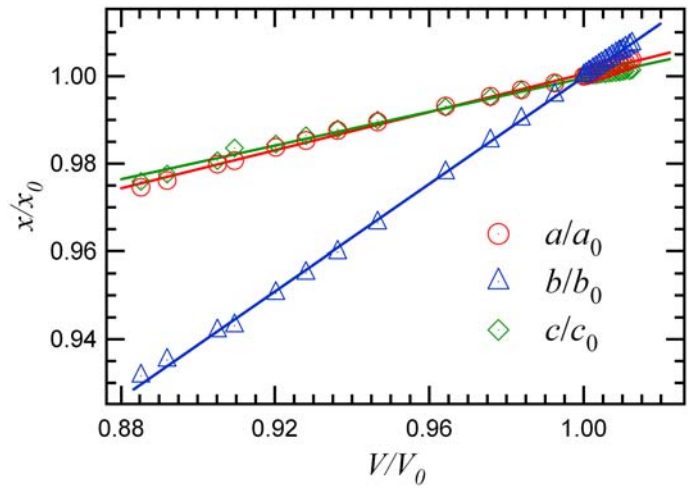

FIG. 4. Normalized unit-cell parameters of adamite plotted against normalized unit-cell volumes. HT dataset ($V/V_0 > 1$): this work; HP dataset ($V/V_0 < 1$): Xu *et al.* (2014).

https://doi.org/10.1180/minmag.2016.080.030 Published online by Cambridge University Press

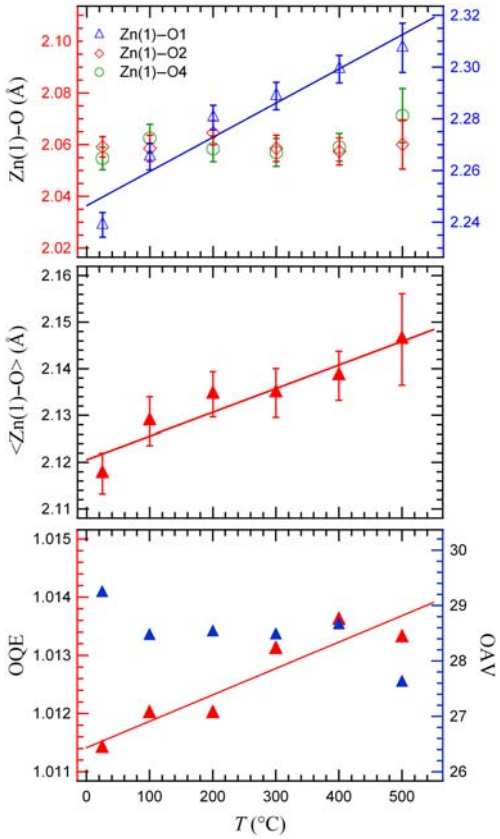

FIG. 5. Geometrical and distortion parameters for the Zn(1) polyhedron as a function of temperature. Upper panel: individual Zn(1)–O bond distances; central panel: Zn(1)–O average distance; lower panel: octahedral quadratic elongation (OQE) and octahedral angular variance (OAV).

Structure refinements

All structure refinements were carried out in space group *Pnnm* by full-matrix least-squares using *SHELXL-97* (Sheldrick, 1998). Note that, differently from libethenite (Zema *et al.*, 2010), unit-cell parameters for adamite are $a > b$ when the same setting is used. Equivalent reflections collected from RT to 400°C were averaged, and the resulting internal agreement factors, R_{int}, are reported in Table 3. Scattering curves for neutral atoms were taken from the *International Tables for X-ray Crystallography* (Ibers and Hamilton, 1974). Structure refinement from data collected at RT was performed starting from the coordinates of Hill (1976). All non-hydrogen atoms were refined anisotropically without constraints. The H atom was located in the difference-Fourier map and its position refined freely with an isotropic displacement parameter fixed at 1.2 times that of its neighbouring oxygen atom. Details of structure refinement from RT data are given in Table 1.

Structure refinements of data collected at different temperatures by the PW1100 diffractometer were carried out starting from the model obtained at the immediately lower temperature. Resolution of HT datasets is lower with respect to data collected at RT; nonetheless, the hydrogen position was still evident in difference-Fourier maps up to 400°C. The hydrogen atom was inserted in the structural models at positions found from the difference Fourier maps. During the refinements, the H coordinates were allowed to ride on the coordinates of the O4 atom with proportional (×1.2 times) isotropic displacement parameters. For all structure refinements, structure factors were weighted according to $w = 1/[\sigma^2(F_o^2) + (AP)^2 + BP]$, where $P = (F_o^2 + 2F_c^2)/3$, and A and B were chosen to produce a flat analysis of variance in terms of F_c^2 as suggested by the program. An extinction parameter x was refined to correct the structure factors according to the equation $F_o = F_c k[1 + 0.001xF_c^2\lambda^3/\sin 2\theta]^{-1/4}$ (where k is the overall scale factor). Such a correction was not applied to the dataset collected at 500°C. All the parameters were refined simultaneously; final difference-Fourier maps were featureless. Values of the conventional agreement indices, R_1 and R_{all}, as well as the goodness of fit (S) based on F^2 are reported in Table 3. Fractional coordinates and anisotropic displacement parameters U^{ij} are reported in Table 4, whereas interatomic distances and selected geometrical parameters are reported in Table 5. Crystallographic information files and lists of observed structure factors have been deposited with the Principal Editors of *Mineralogical Magazine* and are available at www.minersoc.org/pages/e-journals/dep_mat_mm.html.

Results and Discussion

Unit-cell parameters

Unit-cell parameters and volumes of adamite are plotted as a function of temperature in Fig. 2. In the range 25–400°C, adamite shows positive and linear expansion. The thermal expansion coefficients, determined over this temperature range by least-squares linear regression analysis, are

https://doi.org/10.1180/minmag.2016.080.030 Published online by Cambridge University Press

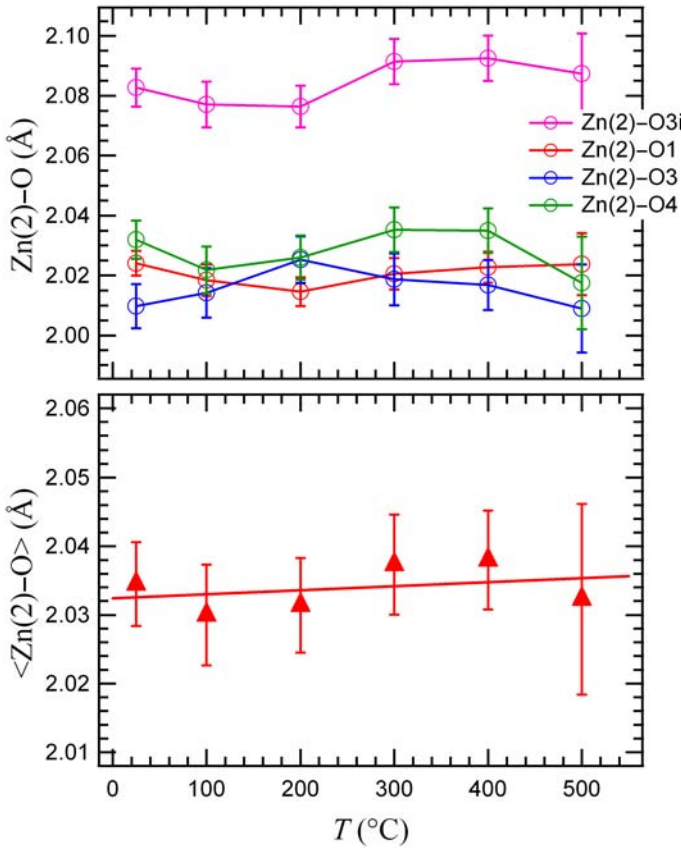

FIG. 6. Geometrical and distortion parameters for the Zn(2) polyhedron as a function of temperature. Upper panel: individual Zn(2)–O bond distances; lower panel: Zn(2)–O average distance.

$\alpha_a = 1.06(2) \times 10^{-5}$ K^{-1}, $\alpha_b = 1.99(2) \times 10^{-5}$ K^{-1}, $\alpha_c = 3.7(1) \times 10^{-6}$ K^{-1} and $\alpha_V = 3.43(3) \times 10^{-5}$ K^{-1}. Axial expansion is strongly anisotropic with α_a:α_b:α_c = 2.86: 5.38 : 1, as evident from Fig. 3, where normalized unit-cell parameters are reported as a function of T (up to 400°C, i.e. until linearity is maintained), and is definitely more anisotropic than in libethenite (Zema *et al.*, 2010). Quantitative estimation of structure-controlled thermal expansion anisotropy was derived using the formalism of Schneider and Eberhard (1990), $A = (|\alpha(b) - \alpha(c)| + |\alpha(b) - \alpha(a)| + |\alpha(c) - \alpha(a)|) \times 10^{-6}$, which yielded a value of 3.2 K^{-1}. Starting from T = 400°C, an abrupt increase of c is observed. This is also accompanied by a slight deviation from linearity in the evolution of a , whereas b does not show significant variation. Concomitantly, the crystal starts deteriorating, diffraction profiles broaden and intensities weaken, indicating incipient dehydration. This process seems to occur at a slightly lower temperature in adamite than in its Cu analogue libethenite (Zema *et al.*, 2010). Linear behaviour is still observed in Stage 2, i.e. after the crystal has undergone partial dehydration (Fig. 2). Axial thermal expansion coefficients in this stage are $\alpha_a = 1.00(3) \times 10^{-5}$ K^{-1}, $\alpha_b = 1.72(5) \times 10^{-5}$ K^{-1}, $\alpha_c = 6.7(1) \times 10^{-6}$ K^{-1} and $\alpha_V = 3.40(4) \times 10^{-5}$ K^{-1}, with α_a:α_b:α_c = 1.49:2.56 : 1.

Unit-cell parameters measured as a function of temperature in this work (Stage 1) have been combined with those measured at high pressure (HP) by Xu *et al.* (2014). Relative lengths are plotted in Fig. 4 as a function of cell volumes. All data are normalized to their relevant RT values. It must be noted here that a and b parameters reported by Xu *et al.* (2014) have been inverted in order to use the same crystallographic setting. As evident from the graph, variations of each individual lattice parameter as a function of cell

https://doi.org/10.1180/minmag.2016.080.030 Published online by Cambridge University Press

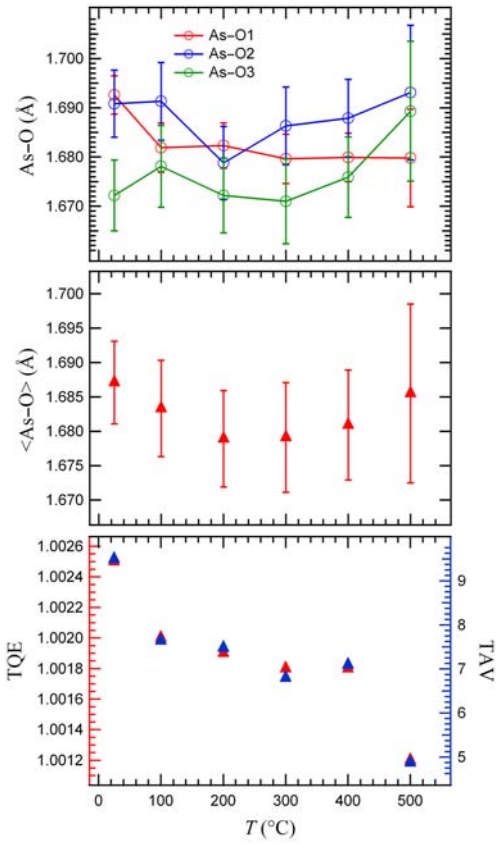

FIG. 7. Geometrical and distortion parameters for As polyhedron as a function of temperature. Upper panel: individual As–O bond distances; central panel: As–O average distance; lower panel: tetrahedral quadratic elongation (TQE) and tetrahedral angular variance (TAV).

volume are linear, thus displaying the so-called 'inverse relationship' (Hazen *et al.*, 2000 and references therein); therefore temperature and pressure behave as structurally analogous variables and the mechanisms of expansion and contraction may be assumed to be the same within this interval. Linear regression analyses over the entire range of investigated cell volume both at HT and HP yielded the following equations:

$$a/a_0 = 0.782(2) + 0.218(2)V/V_0 \left(R^2 = 0.997\right)$$

$$b/b_0 = 0.388(3) + 0.612(3)V/V_0 \left(R^2 = 0.9994\right)$$

$$c/c_0 = 0.806(3) + 0.193(3)V/V_0 \left(R^2 = 0.995\right)$$

By combining the isobaric thermal expansion coefficient (this work) with the isothermal compressibility coefficients (Xu *et al.*, 2014), the following $V(T,P)$ equation of state is obtained.

$$V = V_0 - 0.0106(1) \times P(\text{GPa}) + 3.43(3) \cdot 10^{-5} \times T(\text{K})$$

Structural modifications at HT

Anisotropy of axial thermal expansion in the range 25-400°C can be rationalized in terms of polyhedra connectivity. Expansion is limited mainly by edge sharing Zn(2) dimers along *a* and by edge sharing Zn(1) octahedra chains along *c*; on the other hand, connections of polyhedra along *b*, the direction of maximum expansion, is guaranteed by corner sharing. Geometrical variations of Zn(1) octahedron are summarized in Fig. 5, where individual and mean bond distances as well as distortion parameters are reported as a function of *T*. As temperature increases Zn(1) undergoes a fairly linear expansion, mainly as a consequence of the increase in the Zn(1)–O1 axial bond length. The four basal Zn(1)–O distances do not vary significantly. Therefore the coordination around Zn(1) becomes more and more 4 + 2 in character with increasing *T*. This is also revealed by the increase of the OQE (Octahedral Quadratic Elongation) distortion parameter, whereas the OAV (Octahedral Angle Variance) is not affected by this axial distortion. Both parameters indicate a certain distortion of the Zn^{2+} (a d^{10} cation) octahedron, which is much less distorted compared to that in libethenite, due to the Jahn-Teller effect on Cu^{2+} cations. Zn(2) polyhedra behave almost as rigid units in this structure, and no significant changes in individual and, consequently, average bond lengths are observed (Fig. 6). The AsO_4 tetrahedra do not change significantly in volume as well, but both TQE (tetrahedral quadratic elongation) and TAV (tetrahedral angular variance) distortion parameters indicate that they evolve towards a regularization of their internal and external geometry with *T* (Fig. 7).

When inter-polyhedral connections are considered, it should be noted that due to the larger ionic radius of Zn^{2+} with respect to Cu^{2+}, the crystal structure of adamite is far more expanded than that of libethenite (unit-cell volumes at RT are 429.80(2) Å^3 *vs.* 398.51(2) Å^3). All octahedral O–O edges are quite long at RT and

https://doi.org/10.1180/minmag.2016.080.030 Published online by Cambridge University Press

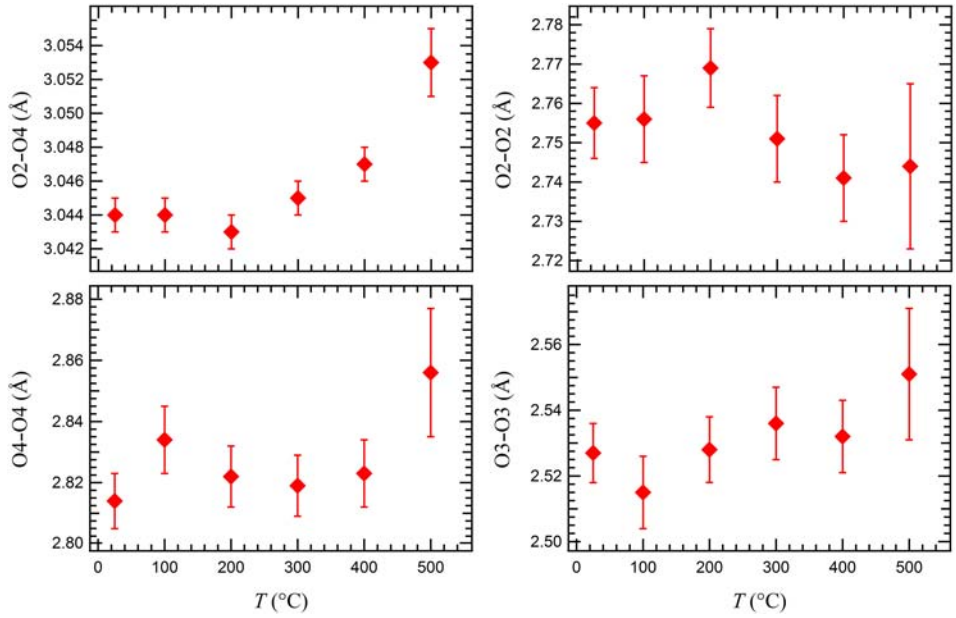

FIG. 8. Variation of selected polyhedral edges with temperature; (*a*) O2–O4, within each octahedron and indicative of the elongation of the chain; (*b*) O2–O2, shared by two octahedra along the chain; (*c*) O4–O4, shared by two octahedra along the chain and bearing the H atoms; (*d*) O3–O3, shared by two Zn(2) trigonal bipyramids. Linear regressions calculated in the range 25–450°C are shown as solid lines.

do not expand further with increasing temperature up to 400°C (Fig. 8). The O3–O3 edge, which is shared by two Zn(2) polyhedra to form the Zn(2)–Zn(2) dimer, is quite short to reduce the high-energy effects of edge sharing and not significantly different from that in libethenite; in the latter case, it increases only slightly with increasing temperature (Fig. 8). As a consequence, Zn···Zn distances also only change slightly (Fig. 9), the Zn(2)···Zn(2) being that showing the largest (and almost linear)

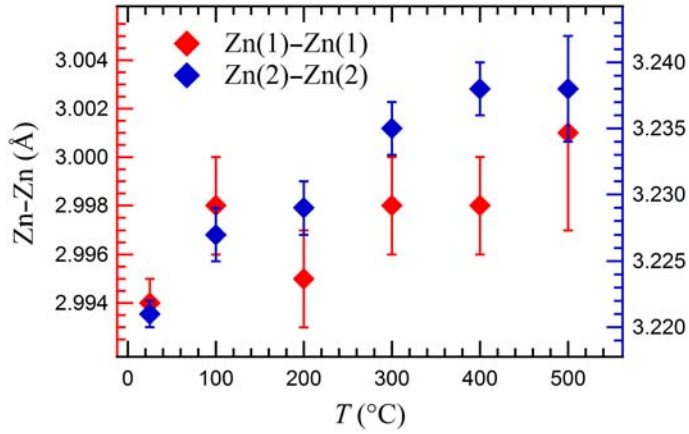

FIG. 9. Cation–cation distances as a function of temperature. Red: Zn(1)–Zn(1) distance along the chain (left axis); Blue: Zn(2)–Zn(2) distance within the dimer (right axis).

https://doi.org/10.1180/minmag.2016.080.030 Published online by Cambridge University Press

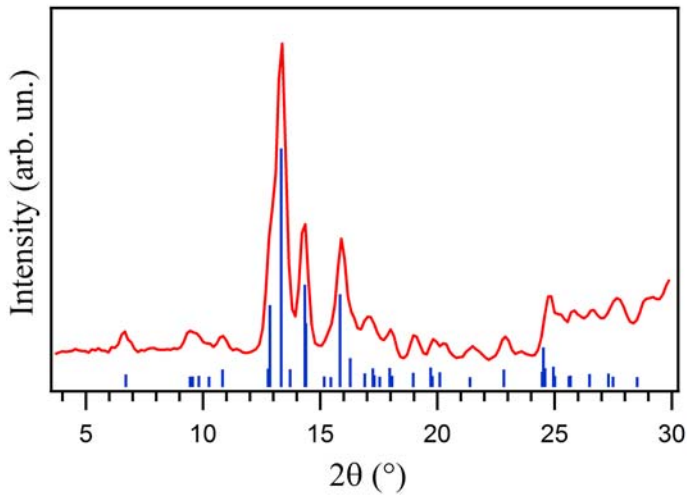

FIG. 10. Mo$K\alpha$ powder X-ray diffraction pattern of the sample at the end of the heating cycles. Red: experimental pattern (a zero shift of –0.2° has been applied); blue: powder diffraction lines relative to $Zn_4(AsO_4)_2O$ (JCPDS code 85-0237).

variation, with an overall increase of <0.02 Å in the range RT to 400°C.

Sudden changes occur at $T = 500$°C, with a dramatic increase in the O2–O4 and O4–O4 edges, associated with an extension of the Zn(1)–O4 bond length. These signs anticipate the breaking of the crystal structure due to dehydration. The process involves the loss of H_2O according to $Zn_4(AsO_4)_2O + H_2O$. At the end of the heating runs, the sample does not behave as a single crystal, but as a polycrystalline aggregate. A final XRD measurement was carried out by rotating it along the φ axis on the CCD diffractometer (detector-to-sample distance = 60 mm; 360°φ rotation; exposure time = 240 s) and diffraction rings were collected. The 1D pattern shown in Fig. 10 is fully indexed by $Zn_4(AsO_4)_2O$ (JCPDS code 85-0237).

Acknowledgements

The authors are grateful to reviewers G.D. Gatta, S.J. Mills and P. Leverett for their valuable suggestions and comments.

References

Blessing, R.H. (1995) An empirical correction for absorption anisotropy. *Acta Crystallographica A*, **51**, 33–38.

Blessing, R.H., Coppens, P. and Becker, P. (1974) Computer analysis of step-scanned X-ray data. *Journal of Applied Crystallography*, **7**, 488–492.

Gaines, R.V., Skinner, H.C.W., Foord, E.E., Mason, B. and Rosenzweig, A. (1997) *Dana's New Mineralogy. The System of Mineralogy of James Dwight Dana and Edward Salisbury Dana.* 8th Edition. John Wiley and Sons, Inc., New York.

Hawthorne, F.C. (1976) A refinement of the crystal structure of adamite. *The Canadian Mineralogist*, **14**, 143–148.

Hazen, R.M., Downs, R.T. and Prewitt, C.T. (2000) Principles of comparative crystal chemistry. Pp. 1–33 in: *High-Temperature and High Pressure Crystal Chemistry* (R.M. Hazen and R.T. Downs, editors). Reviews in Mineralogy and Geochemistry, **41**. Mineralogical Society of America, Washington, DC.

Hill, R.J. (1976) The crystals structure and infrared properties of adamite. *American Mineralogist*, **61**, 979–986.

Ibers, J.A. and Hamilton, W.C. (1974) *International Tables for X-ray Crystallography.* Kynoch Press, Birmingham, UK.

Kato, T. and Y. Miura (1977) The crystal structures of adamite and paradamite. *Mineralogical Journal*, **8**, 320–328.

Kokkoros, P. (1937) Über die Struktur von Adamin. *Zeitschrift für Kristallographie*, **96**, 417–434.

Lehman, M.S. and Larsen, F.K. (1974) A method for location of the peaks in step-scan measured Bragg reflections. *Acta Crystallographica A*, **30**, 580–584.

Makreski, P., Jovanovski, S., Pejov, L., Kloess, G., Hoebler, H.J. and Jovanovski, G. (2013) Theoretical and experimental study of the vibrational spectra of sarkinite $Mn_2(AsO_4)(OH)$ and adamite $Zn_2(AsO_4)(OH)$. *Spectrochimica Acta Part A: Molecular and Biomolecular Spectroscopy*, **113**, 37–42.

Mills, S.J., Kampf, A.R., Poirier, G., Raudsepp, M. and Steele, I.M. (2010) Auriacusite, $Fe^{3+}Cu^{2+}AsO_4O$, the first M^{3+} member of the olivenite group, from the

https://doi.org/10.1180/minmag.2016.080.030 Published online by Cambridge University Press

Black Pine mine, Montana, USA. *Mineralogy and Petrology*, **99**, 113–120.

North, A.C.T., Phillips, D.C. and Mathews, F.S. (1968) A semi-empirical method of absorption correction. *Acta Crystallographica*, **A24**, 351–359.

Schneider, H. and Eberhard, E. (1990) Thermal expansion of mullite. *Journal of the American Ceramic Society*, **73**, 2073–2076.

Sheldrick, G.M. (1998) *SHELX97 – Programs for Crystal Structure Analysis (Release 97-2).* Institut für Anorganische Chemie der Universität, Göttingen, Germany.

Sheldrick, G.M. (2003) *SADABS.* University of Göttingen, Germany.

Toman, K. (1978) Ordering in olivenite–adamite solid solutions. *Acta Crystallographica*, **34**, 715–721.

Xu, J., Ma, M., Wei, S., Hu, X., Liu, Y., Liu, J., Fan, D. and Xie, H. (2014) Equation of state of adamite up to 11 GPa: a synchrotron X-ray diffraction study. *Physics and Chemistry of Minerals*, **41**, 547–554.

Zema, M., Tarantino, S.C. and Callegari, A.M. (2010) Thermal behaviour of libethenite from room temperature up to dehydration. *Mineralogical Magazine*, **74**, 553–565.

https://doi.org/10.1180/minmag.2016.080.030 Published online by Cambridge University Press